NATIONAL AERONAUTICS AND SPACE ADMINISTRATION

TECHNICAL MEMORANDUM X-311

A WIND-TUNNEL INVESTIGATION OF THE AERODYNAMIC CHARACTERISTICS OF BODIES OF REVOLUTION AT MACH NUMBERS OF 2.37, 2.98, AND 3.90 AT ANGLES OF ATTACK TO 90°*

By Fred M. Smith

SUMMARY

An experimental investigation has been conducted on bodies of revolution in the langley high Mach number jet at Mach numbers of 2.37, 2.98, and 3.90 and Reynolds numbers of 0.98×10^6 to 1.37×10^6 per inch at angles of attack to 90°. The investigation was made to determine the effects on the high-angle aerodynamic characteristics produced by blunting a pointed ogival nose to hemispherical, by changing the face shape of a cylindrical nose from concave hemispherical to convex hemispherical, and by adding afterbodies of several lengths to the noses.

Results indicate that the force and stability characteristics were more dependent upon the planform area and area distribution than upon the particular shape or bluntness of the noses. The cross-flow drag theory, used to correlate the experimental normal-force data, accounted for angle of attack and stream Mach number for the tests of a flat-face circular cylinder.

In comparisons of the experimental results with the results from several variations of Newtonian impact theory, the unmodified theory most accurately (not satisfactorily) predicted the experimental results.

INTRODUCTION

Numerous wind-tunnel investigations have been made to determine the aerodynamic characteristics of bodies of revolution having simple, basic

*Title, Unclassified.

shapes at supersonic speeds for angles of attack to 25° (refs. 1 to 9, for example), but few experimental investigations have been made on bodies with these shapes at angles of attack much above 30° or 40° (refs. 10 and 11). Data from such high-angle investigations would have application in the design of missiles which could be fired from supersonic aircraft normal to the airstream, or in the design of ballistic missiles which might reenter the earth's atmosphere at attitudes approaching 90°. In any investigation involving flight at supersonic speeds, the effects of aerodynamic heating must be considered, and consideration of this factor requires a certain amount of blunting for nose survival at supersonic speeds. To determine the effect of this nose bluntness on the aerodynamic characteristics of missile-like configurations, a low-angle (0° to 25°) investigation was conducted on bodies of revolution in earlier wind-tunnel tests wherein a systematic variation in nose bluntness was studied. Results of this investigation were reported in reference 9.

In order to determine the high-angle aerodynamic characteristics of the models of reference 9 and, thereby, provide insight into the high-angle aerodynamic problems, the investigation of reference 9 has been extended to include tests at angles of attack to 90°. These additional tests were made with the same models described in reference 9 at angles of attack of 30° to 90°, Mach numbers of 2.37, 2.98, and 3.90, and Reynolds numbers of 2.9×10^6 to 12.3×10^6 based on body length.

SYMBOLS

The forces and moments of the present investigation are referred to the body axes, and the reference center of moments is located at the 50-percent body-length station, regardless of whether the body consists of a nose configuration alone or a nose configuration in combination with an afterbody.

A body frontal area, $\frac{\pi d^2}{4}$

$C_{D,c}$ cross-flow drag coefficient, $\frac{F_N}{q_N S}$

C_m pitching-moment coefficient about 0.5l, $\frac{\text{Pitching moment}}{qAd}$

$C_{m'}$ pitching-moment coefficient based on planform area, $\frac{\text{Pitching moment}}{qSd}$

C_N	normal-force coefficient, $\frac{F_N}{qA}$
C_N'	normal-force coefficient based on planform area, $\frac{F_N}{qS}$
d	maximum body diameter
d/2r	face shape ratio (used with the cylindrical-nose configurations)
F_N	normal force
l	total body length (may be nose alone or nose plus afterbody)
l_A	afterbody length
l_N	nose length
M	free-stream Mach number
M_N	normal or cross-flow Mach number, M sin α
p	free-stream static pressure
$p_{t,1}$	stagnation pressure in front of normal shock
$p_{t,2}$	stagnation pressure behind normal shock
q	free-stream dynamic pressure, $\frac{\gamma}{2} pM^2$
q_N	normal or cross-flow dynamic pressure, $\frac{\gamma}{2} pM_N^2$
r	tip radius of ogival noses and face radius of cylindrical noses (fig. 1)
2r/d	nose bluntness ratio (used with the ogival-nose configurations)
R	radius of curvature (fig. 1)
S	body planform area
x	center-of-pressure location, measured from nose

4 [redacted]

α angle of attack

γ ratio of specific heats of air

APPARATUS AND TESTS

The tests were conducted in the Langley high Mach number jet for which Mach number variations were obtained with interchangeable nozzles. The Mach numbers and other test variables are given in the following table:

M	$p_{t,1}$, lb/sq in. abs	Reynolds number per inch
2.37	50	0.98×10^6
2.98	75	1.09
3.90	150	1.37

The stagnation temperature varied from approximately 75° F to approximately 30° F during each test. The Reynolds numbers were computed for an average temperature of 50° F. The models were sting-mounted on a two-component internal strain-gage balance which was used to measure normal force and pitching moment. The angle-of-attack range of 30° to 90° was covered in 15° increments by inserting the model sting into blocks, each of which had a hole bored at one of the angles of attack. These blocks were mounted in a plate on the tunnel sidewall and were set before each test was begun. The angles of attack were corrected for sting deflections under load.

Tests were made with air having less than 5×10^{-6} pounds of water per pound of dry air, which eliminated water-condensation effects. The test-section static temperature and pressure did not reach values for which liquefaction would occur.

MODELS

The models of this investigation (figs. 1 and 2) were the same as those described in reference 9. The fineness-ratio-5 afterbody was too long for the tunnel test section at the high angles of the present investigation and was necessarily omitted from the testing. Two series of

nose configurations were tested; the first series, identified herein as ogival (fig. 1(a)), had profiles formed by circular arcs tangent at the tips to spheres with radii r of 0, 0.10, 0.20, and 0.50 the maximum body radius d/2 and tangent at the rearward end to the maximum body diameter. The second series of noses (fig. 1(b)) consisted of right-circular cylinders (infinite ogives) with convex, flat, and concave faces and in the strictest sense could not be classed as noses but in this discussion are designated as cylindrical noses. The cylindrical nose with the convex hemispherical face is discussed with both series of noses and serves as the end-point configuration of both series.

In order to determine the effect of nose length (nose fineness ratio l_N/d), three of the ogival noses with the same bluntness ratio ($2r/d = 0.20$) had fineness ratios of 3, 5, and 7. All the other noses had nominal fineness ratios of 5. The noses were tested alone and in combination with cylindrical afterbodies (fig. 1(c)) having fineness ratios l_A/d of 1, 2, and 3 for a range of overall fineness ratio l/d of 3 to 9.

ACCURACY

The maximum inaccuracies of the experimental angles, force coefficients, and moment coefficients, due to balance and readout equipment limitations, and the average repeatability of the system have been estimated and are presented in the following table:

α, deg	±0.25
C_N, $C_{D,c}$	±0.150
C_N'	±0.050
C_m	±0.150
C_m'	±0.050

RESULTS AND DISCUSSION

Pitching-moment and normal-force coefficients are presented in figures 3 and 4 as functions of angle of attack and in figures 5 and 6 as functions of nose bluntness and nose shape. The geometric parameter used to define the ogival-nose bluntness is $2r/d$ (called the nose bluntness ratio), and the geometric parameter used to define the cylindrical nose shape is $d/2r$ (called the face shape ratio). The inverse of the nose bluntness ratio was used for the cylindrical noses to avoid the problem of plotting infinity. Figure 7 presents a correlation of

experimental C_m and C_N for several models based on planform area. Nondimensional centers of pressure are given in figures 8 and 9 as functions of angle of attack, nose bluntness, and nose face shape. Figures 10 and 11 present C_m and C_N for several configurations as functions of afterbody length and nose length. Figure 12 presents a comparison of experimental and theoretical normal force for several representative configurations. Figure 13 presents a correlation of the experimental normal-force data for the flat-face circular cylinder. In this figure the cross-flow drag coefficient is plotted against the cross-flow (normal) Mach number.

Nose Bluntness

The effects of nose bluntness on the aerodynamic characteristics of several ogival noses alone and in combination with a fineness-ratio-2 afterbody are shown in figures 3, 5, 8(a), and 9(a) for the three Mach numbers.

Normal force.- Figures 3 and 5 show that increasing the nose bluntness from pointed ogival to hemispherical produces large increases in C_N (up to 55 per cent at $\alpha = 90^\circ$, $M = 2.98$, fig. 3(a)). The magnitude of the increase is shown to be approximately the same for the noses alone (figs. 3(a) and 5(a)) as it is for the noses in combination with a fineness-ratio-2 afterbody (figs. 3(b) and 5(b)). This similarity indicates that bluntness effects on the carryover normal force from the noses to the afterbodies are small. The curves of figure 5 show that the increase in C_N is essentially linear with increasing nose bluntness. Because the nose planform area also increases approximately linearly with increasing nose bluntness, the increase in C_N is assumed to result from the increased area, especially at the higher angles of attack. Figure 7 presents further evidence that the normal force for bodies of revolution is dependent upon the planform area of the bodies. Shown in this figure are data for the pointed ogival nose with and without a fineness-ratio-2 afterbody, along with the data for the flat-face circular cylinder, also with and without the fineness-ratio-2 afterbody. When referred to the body frontal area (unflagged symbols, unprimed coefficients) the data for the four configurations are widely spread, but when referred to the planform area (flagged symbols, primed coefficients) the spread between the data diminishes and the data very nearly collapse into one curve.

Pitching moment and center of pressure.- There are some inconsistencies in C_m for the noses alone (figs. 3(a) and 5(a)) so that stability of a nose at a particular point is in doubt. In general, however, it appears that the noses alone are almost neutrally stable, with the bluntest noses being slightly unstable and the sharpest noses being slightly

stable. The effects of bluntness are more clearly shown in figure 3(b) in which the noses are combined with a fineness-ratio-2 afterbody for which each increase in nose bluntness provides an accompanying decrease in stability. The reason for this result is explained by the fact that an increase in nose bluntness contributes planform area ahead of the center of moments. An illustration of the effects on the center of pressure of increasing the nose bluntness is shown in figures 8(a) and 9(a) where, as in reference 9, the center of pressure generally moves forward with each increase in bluntness. An exception to this trend was noted for the hemispherical nose for which the center of pressure moved slightly rearward. Also shown in figure 8(a) is the trend of rearward movement in center of pressure toward the centroid of planform area with increasing angle of attack. This result is attributed to the fact that the angle-of-attack effects outweigh the effects of local surface slope. The trend was noted in reference 2, but the angles of attack were too low for positive stability to be reached.

Face Shape

The effects of face shape on the aerodynamic characteristics of cylindrical noses alone and in combination with a fineness-ratio-2 afterbody are presented in figures 4, 6, 8(b), and 9(b). Face shape is defined for the cylindrical noses as the ratio of the radius of the base to the radius of the nose face profile $d/2r$.

Normal force.- Figures 4 and 6 indicate that C_N is essentially unaffected by the face shape variation of this investigation. From planform-area considerations this result would be expected because the difference in areas is less than $2\frac{1}{2}$ percent.

Pitching moment and center of pressure.- The plots of C_m against α in figure 4 reveal that in general the cylindrical-nose configurations appear to be stable for the angles of attack of this investigation. As might be expected, the noses with the convex faces (positive $d/2r$) in general possess greater stability about the 50-percent body-length station than those with the concave faces (negative $d/2r$) because there is less planform area for the former forward of the reference center of moments. Specifically, figure 6, which presents C_m plotted against face shape ratio $d/2r$, shows a slight negative increase in C_m with increasing $d/2r$ for given angles of attack. This negative increase in C_m is also shown in figure 4. The center-of-pressure results (figs. 8(b) and 9(b)) show the same trend in that the center of pressure moves rearward with increasing angle of attack and, less obviously, with increasing face shape ratio.

Afterbody Length or Fineness Ratio

The effects of variation in afterbody length on C_m and C_N for the nose configurations of this investigation may be seen in figures 3 to 7 and in figures 10 and 11. With each increase in afterbody length the reference center of moments was shifted to the new 50-percent body-length station. An increase in afterbody length does not necessarily, therefore, produce an automatic stabilizing increment in pitching moment.

Normal force.- Figures 3 to 6 and 11 show that the addition of an afterbody produces increments in C_N for all configurations and, in addition, tends to reduce slight irregularities in the C_N curves. (Compare the curves of figs. 3(a) and 3(b).) Figure 10 shows, as does figure 7, that the afterbodies produce normal force proportional to their planform area since in figure 10 C_N increases for the ogival nose ($2r/d = 0.2$) almost linearly with increasing body length.

Pitching moment and center of pressure.- In general, increased afterbody length for the ogival noses (figs. 3, 5, 7, 10, and 11) results in a small stabilizing increment in C_m because of the rearward shift in centers of pressure (figs. 8(a) and 9(a)). Increased afterbody length for the cylindrical noses (figs. 4, 6, and 7) has no appreciable effect on C_m, because the nondimensional centers of pressure do not change with additional body length (figs. 8(b) and 9(b)). As the center of pressure apparently moves with changes in the center of area, it is easily understood why the ogival noses experience changes and the cylindrical noses do not.

Nose Length

The effects of variation in nose length on the aerodynamic characteristics of an ogival nose ($2r/d = 0.2$) are shown in figure 11, in which C_N increases with increasing nose length. This trend is an extension of that established in reference 9 for angles of attack greater than about 10°. It was also established that for angles of attack less than about 10°, the fineness-ratio-3 nose (although shorter and smaller in planform area than the fineness-ratio-5 nose by about 40 percent and than the fineness-ratio-7 nose by about 60 percent) apparently, because of its greater local surface slope, produced C_N equal to approximately that for the latter two configurations. Also in reference 9 it was concluded that the longer noses possessed greater static stability than the shorter ones because they more closely approached a stable conical configuration. In the present investigation, however, as shown for the plots of C_m in figure 11, the fineness-ratio-5 nose apparently possesses

less static stability than either the fineness-ratio-3 or the fineness-ratio-7 nose, a result not reconciled by the conclusions of reference 9.

Theoretical Comparisons

Comparisons of experimental and theoretical C_N for three noses, representative of the configurations of this investigation, are shown in figure 12 as functions of α. The theoretical values of C_N were obtained from flat-plate Newtonian theory ($2 \sin^2\alpha$), circular-body Newtonian theory $\left(\frac{16}{3\pi} \sin^2\alpha, \text{ ref. 12}\right)$, and modified circular-body Newtonian theory $\left(\frac{p_{t,2} - p}{q} \frac{16}{6\pi} \sin^2\alpha, \text{ where } \frac{p_{t,2} - p}{q} \text{ is the theoretical stagnation-pressure coefficient (ref. 13), and } \frac{16}{6\pi} \text{ is the inverse ratio of the first two methods used to adapt this theory for application to circular bodies}\right)$. The modified Newtonian theory was applied to the pointed ogival nose (fig. 12(a)) and the hemispherically faced cylindrical nose (fig. 12(b)) by use of the method in reference 14. This method is very useful in determining local surface slopes and in determining integrated pressure coefficients for bodies with curved profiles. The third nose of the group, the flat-face cylinder, is shown in figure 12(c). Unfortunately, the agreement between experiment and theory is rather poor for the three noses in figure 12, as well as for the remaining noses of the investigation. Flat-plate theory, as expected, overestimates C_N for all three noses, especially at the higher angles of attack and higher Mach number. Modified Newtonian, which is presented only for $M = 2.37$ and $M = 3.90$, underestimates C_N for all three noses and the same is true for the unmodified Newtonian theory. It can be seen, however, that although none of the predictions are accurate, the unmodified Newtonian theory does come closer to predicting the experimental results than the other methods, particularly at the two upper Mach numbers.

The normal force coefficient for the flat-face circular cylinder is plotted in figure 13(a) as a function of stream Mach number for angles of attack of 30°, 60°, and 90°. With data from reference 10 included, the Mach number range extends from 2.37 to 6.86. Also presented in figure 13(a) are additional predictions from the modified and unmodified Newtonian theories. Because these are essentially hypersonic theories, the poor agreement between the experimental and theoretical results in figures 12 and 13(a) (for $M < 4$), and the good agreement between experiment and theory for $M > 4$ in figure 13(a) is about as expected.

[redacted]

Cross-Flow Drag Correlation

The normal-force values of figure 13(a) have been referenced to a dynamic pressure based on the cross-flow or normal Mach number and replotted in figure 13(b) as the cross-flow drag coefficient (ref. 10) against the normal Mach number. This causes all the data to collapse into more or less one curve, still in agreement with Newtonian theory for $M_N > 3.5$ or 4. It may be worth noting that the experimental $C_{D,c}$ is approximately constant also for $M_N > 3.5$ or 4.

It is interesting to note that the cross-flow drag correlation and the Newtonian theory are similar in that they are both based on the thesis that the momentum of the normal component of a supersonic air stream produces the force on a body of revolution immersed in the stream. They are dissimilar in that Newtonian theory utilizes a theoretical maximum pressure coefficient at $\alpha = 90^\circ$ to determine a pressure or force coefficient at angles other than 90°, whereas the cross-flow drag correlation utilizes an experimental pressure or force coefficient at a particular angle of attack to determine an equivalent maximum force or pressure coefficient at $\alpha = 90^\circ$.

The experimental cross-flow drag curve of figure 13(b) can be used to estimate the normal force for a circular cylinder at any stream Mach number (greater than the normal Mach number) and the appropriate angle of attack by the simple relationships $M_N = M \sin \alpha$, $C_N' = \dfrac{F_N}{\frac{\gamma}{2} pM^2 S}$, and

$$C_{D,c} = \frac{F_N}{\frac{\gamma}{2} pM_N^2 S}.$$

CONCLUSIONS

A wind-tunnel investigation of the aerodynamic characteristics of a group of ogival-nose configurations with varying nose bluntness and a group of cylindrical-nose configurations with varying face shape in combination with afterbodies having fineness ratios of 1, 2, and 3 was made in the Langley high Mach number jet at Mach numbers of 2.37, 2.98, and 3.90 at angles of attack of 30° to 90° and resulted in the following conclusions:

1. In general, the noses were more dependent upon planform area than upon nose bluntness or face shape for the magnitude of the normal force, particularly at the highest angles.

[redacted]

2. The stability of [redacted] noses and the nose-afterbody combinations appears to depend more on the distribution of the planform area than on the nose shape or nose roundness; for this investigation the cylindrical-nose configurations were generally stable.

3. The cross-flow drag, used to correlate the experimental normal-force data for a flat-face circular cylinder, accounted for angle-of-attack effects and stream Mach number.

4. The experimental data for three representative configurations were compared with the results of flat-plate Newtonian theory, Newtonian theory, and modified Newtonian theory (the latter two methods were designated as circular-cylinder methods); although none of the comparisons were satisfactory, the unmodified Newtonian theory resulted in the best overall agreement.

Langley Research Center,
National Aeronautics and Space Administration,
Langley Field, Va., May 27, 1960.

1. Cooper, Ralph D., and Robinson, Raymond A.: An Investigation of the Aerodynamic Characteristics of a Series of Cone-Cylinder Configurations at a Mach Number of 6.86. NACA RM L51J09, 1951.

2. Dennis, David H., and Cunningham, Bernard E.: Forces and Moments on Pointed and Blunt-Nosed Bodies of Revolution at Mach Numbers From 2.75 to 5.00. NACA RM A52E22, 1952.

3. Dennis, David H., and Cunningham, Bernard E.: Forces and Moments on Inclined Bodies at Mach Numbers From 3.0 to 6.3. NACA RM A54E03, 1954.

4. Neice, Stanford E., and Wong, Thomas J.: An Experimental Investigation of the Applicability of the Hypersonic Similarity Law to Bodies of Revolution. NACA RM A52K07, 1953.

5. Syvertson, Clarence A., and Dennis, David H.: A Second-Order Shock-Expansion Method Applicable to Bodies of Revolution Near Zero Lift. NACA Rep. 1328, 1957. (Supersedes NACA TN 3527.)

6. Smith, Fred M., Ulmann, Edward F., and Dunning, Robert W.: Longitudinal and Lateral Aerodynamic Characteristics at Combined Angles of Attack and Sideslip of a Generalized Missile Model Having a Rectangular Wing at a Mach Number of 4.08. NACA RM L58E26, 1958.

7. DeLancey, L. M., and Jaeger, B. F.: The Aerodynamic Characteristics at Mach Number 4.24 of 14- and 18-Caliber Rocket Models With Folding Fins. NAVORD Rep. 2010 (NOTS 631), U.S. Naval Ord. Test Station, Inyokern (China Lake, Calif.), Jan. 30, 1953.

8. Brown, C. S., Luther, M. L., and Schroedter, G. M.: Experimental Studies of Forces, Pressure Distributions, and Viscous Effects on Long Inclined Bodies of Revolution at Mach 2.96. NAVORD Rep. 1281 (NOTS 351), U.S. Naval Ord. Test Station, Inyokern (China Lake, Calif.), Feb. 12, 1951.

9. Smith, Fred M.: A Wind-Tunnel Investigation of Effects of Nose Bluntness, Face Shape, and Afterbody Length on the Aerodynamic Characteristics of Bodies of Revolution at Mach Numbers of 2.37, 2.98, and 3.90. NASA TM X-230, 1960.

10. Penland, Jim A.: Aerodynamic Characteristics of a Circular Cylinder at Mach Number 6.86 and Angles of Attack Up to 90°. NACA TN 3861, 1957. (Supersedes NACA RM L54A14.)

11. Brindle, C. Carl: Longitudinal Characteristics at Supersonic Speeds of a Winged and a Wingless 0.08-Scale Half Model Sparrow I Missile at Angles of Attack Up to 180°. Aero Rep. 931, David W. Taylor Model Basin, Navy Dept., Dec. 1957.

12. Grimminger, G., Williams, E. P., and Young, G. B. W.: Lift on Inclined Bodies of Revolution in Hypersonic Flow. Jour. Aero. Sci., vol. 17, no 11, Nov. 1950, pp. 675-690.

13. Ames Research Staff: Equations, Tables, and Charts for Compressible Flow. NACA Rep. 1135, 1953. (Supersedes NACA TN 1428.)

14. Rainey, Robert W.: Working Charts for Rapid Prediction of Force and Pressure Coefficients on Arbitrary Bodies of Revolution by Use of Newtonian Concepts. NASA TN D-176, 1959.

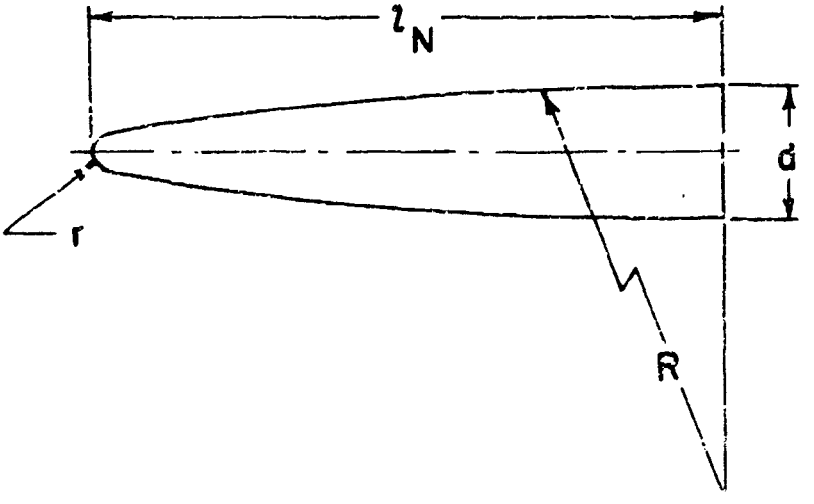

Nose	R	l_N	d	r	l_N/d	2r/d	S
1	25.25	4.986	1.000	0	5.	0	3.340
2	27.51	5.009	1.001	.[illegible]	5.0	0.10	3.476
3	10.81	2.995	1.001	.10	3.0	0.20	2.155
4	30.34	5.060	.998	.10	[illegible].1	20	3.614
5	59.81	7.051	1.000	.10	7.0[illegible]	[illegible].20	5.080
6	45.75	4.980	1.001	.[illegible]	5.0	0.50	4.065
7	∞	5.009	1.002	.50	5.0	1.00	4.893

(a) Ogival noses.

Figure 1.- Geometric characteristics of the model components. Dimensions are in inches.

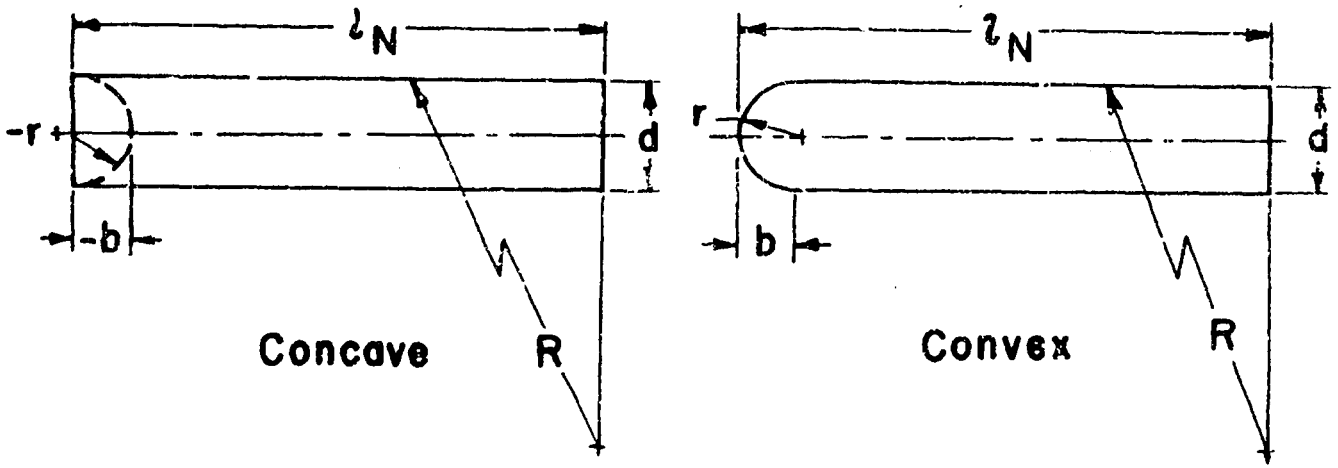

Nose	R	l_N	d	r	b	l_N/d	d/2r	S
7	∞	5.009	1.002	.50	.50	5.0	1.0	4.893
8	∞	5.011	1.001	.625	.25	5.0	.8	4.925
9	∞	5.010	1.001	∞	0	5.0	0	5.015
10	∞	5.010	1.001	-.625	-.25	5.0	-.8	5.015
11	∞	5.000	1.001	-.50	-.50	5.0	-1.0	5.005

(b) Cylindrical noses.

Figure 1.- Continued.

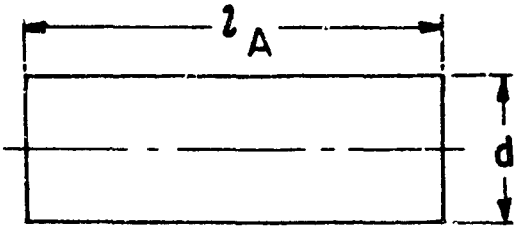

Afterbody	l_A	d	l_A/d
1	1.002	1.000	1.0
2	2.005	1.000	2.0
3	3.007	1.002	3.0

(c) Afterbodies.

Figure 1.- Concluded.

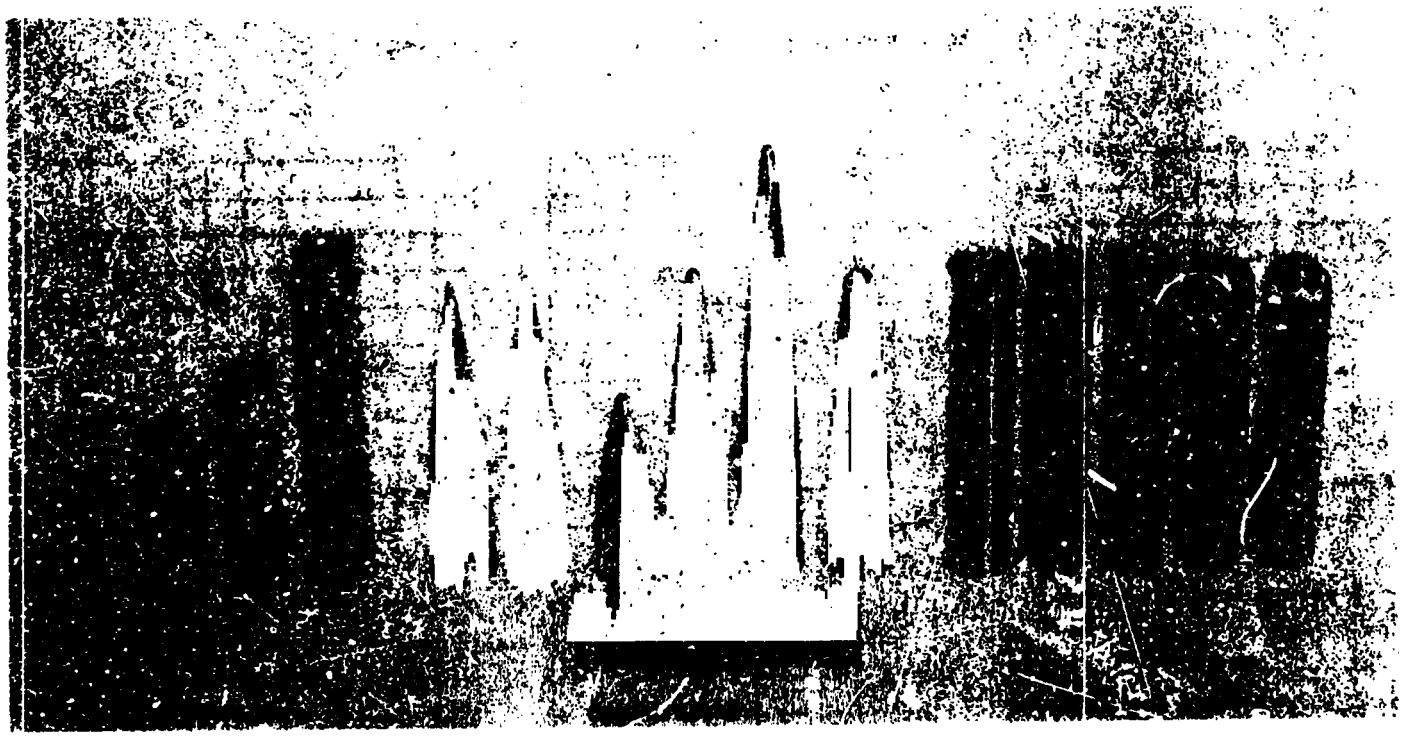

L-58-720.1

Figure 2.- Photograph of the model components.

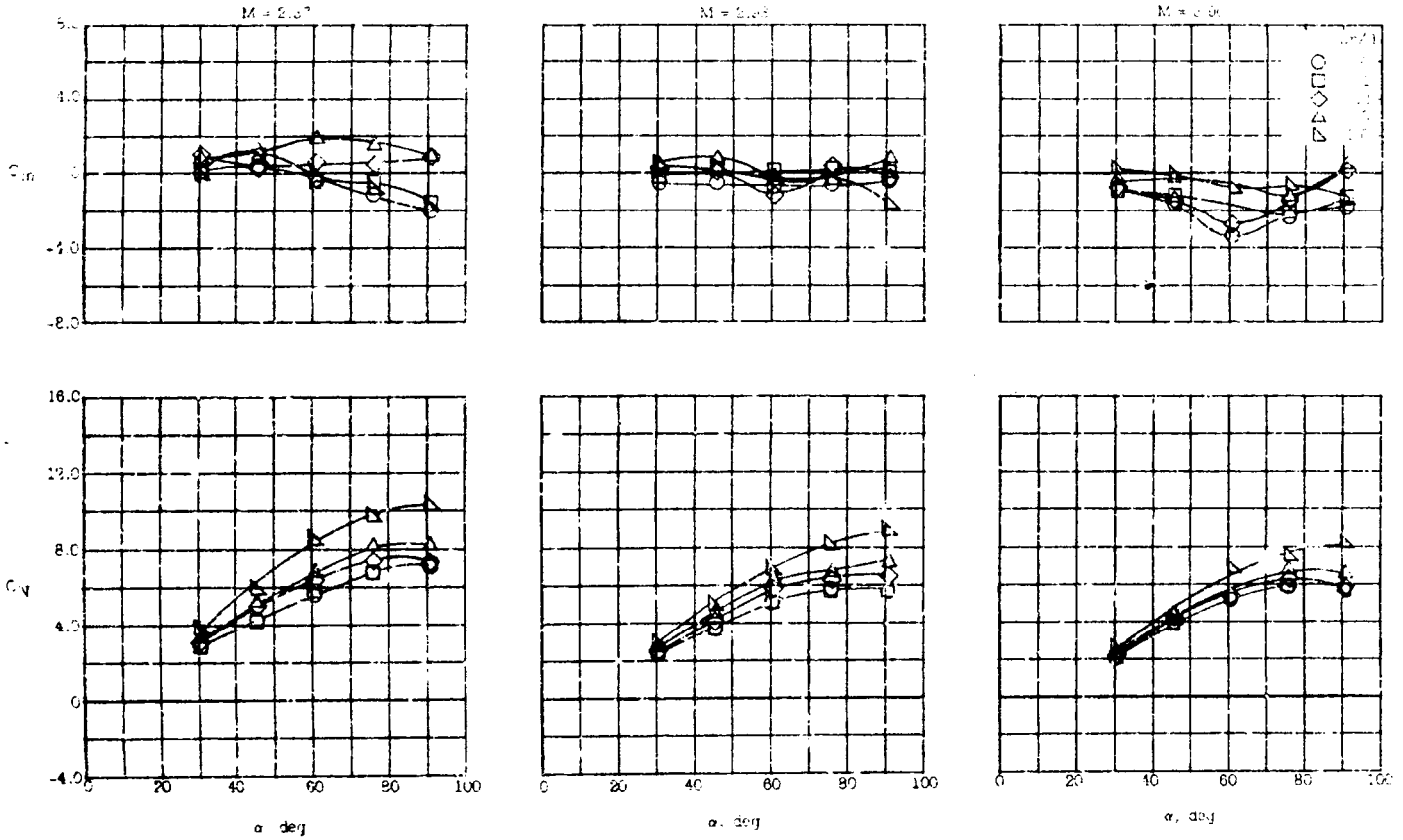

(a) Ogival noses alone. $l/d = l_N/d = 5$.

Figure 3.- Effects of nose bluntness variation on C_m and C_N for fineness-ratio-5 ogival noses with and without a fineness-ratio-2 cylindrical afterbody.

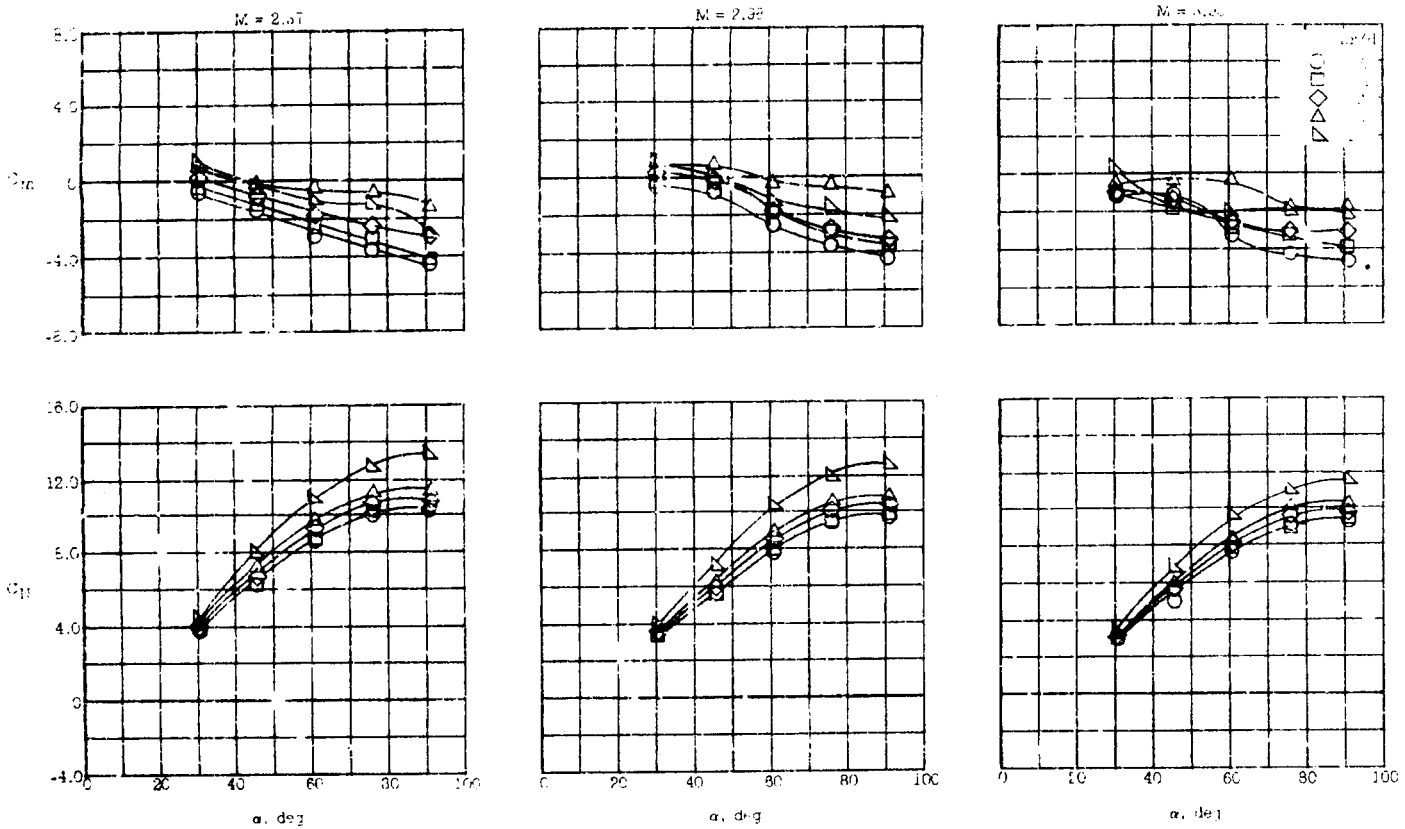

(b) Ogival noses combined with a fineness-ratio-2 cylindrical afterbody. $l/d = 7$; $l_N/d = 5$.

Figure 3.- Concluded.

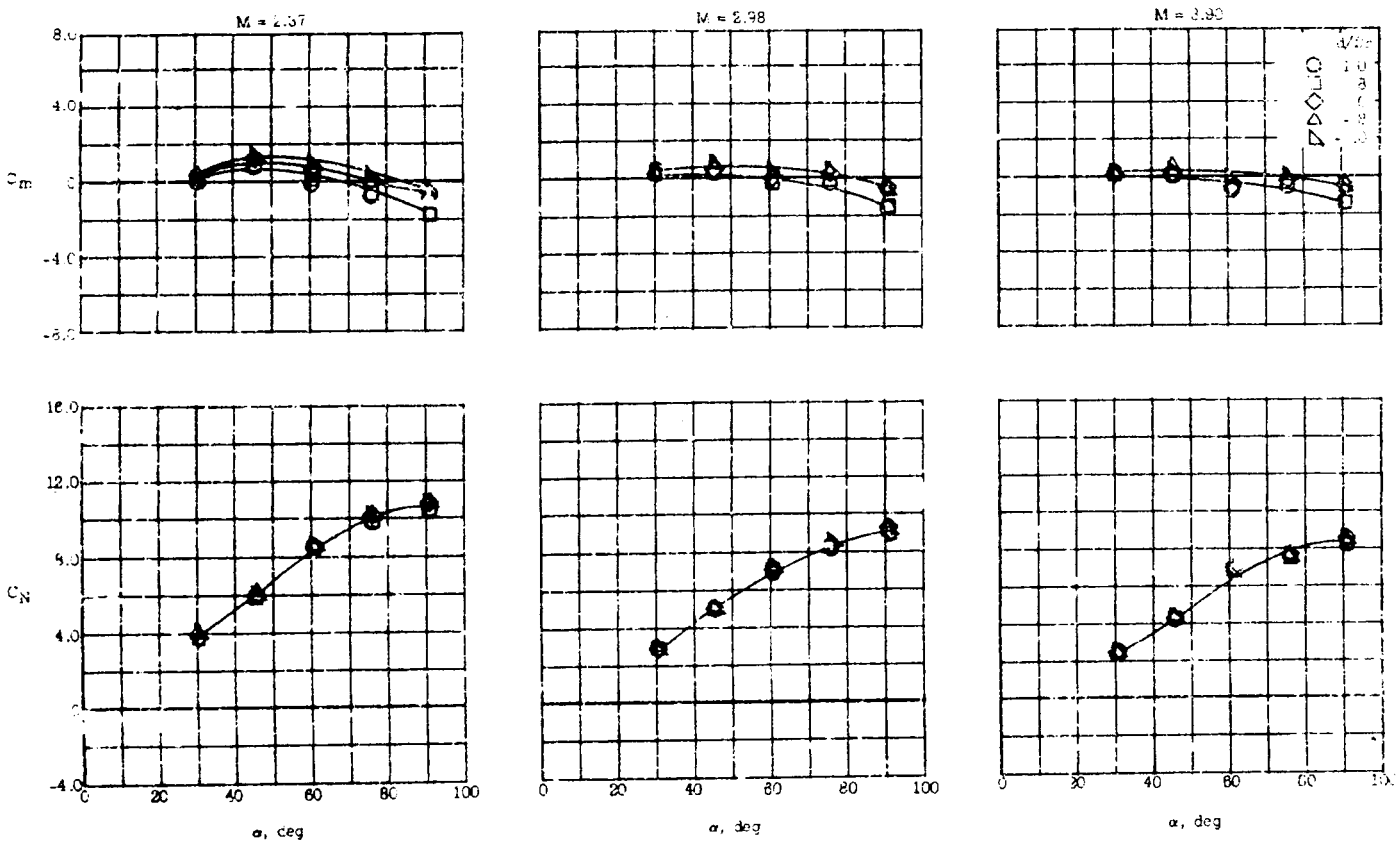

(a) Cylindrical noses alone. $l/d = l_N/d = 5$.

Figure 4.- Effects of face shape variation on C_m and C_N for fineness-ratio-5 cylindrical noses with and without a fineness-ratio-2 cylindrical afterbody.

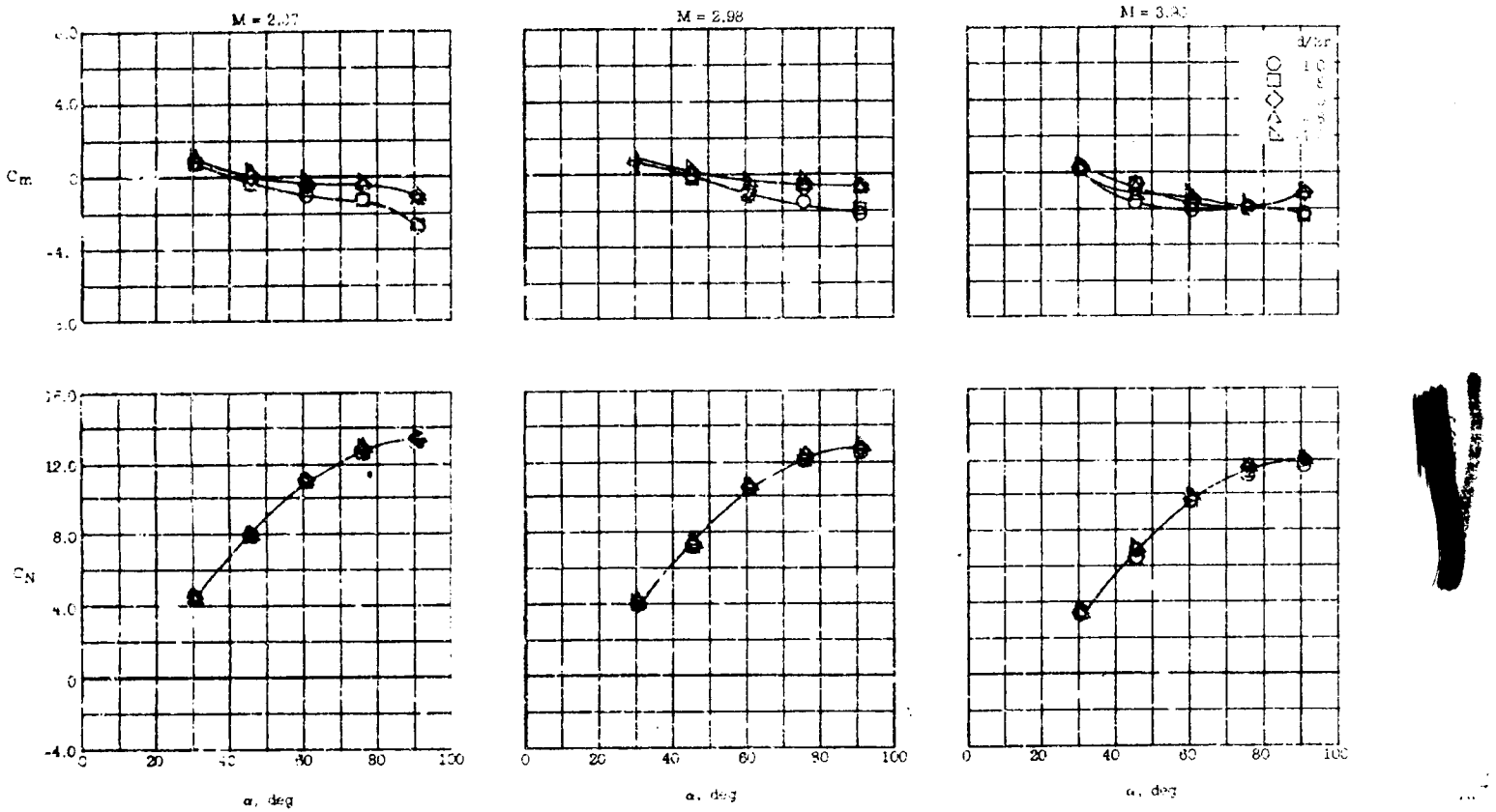

(b) Cylindrical noses combined with a fineness-ratio-2 cylindrical afterbody. $l/d = 7$; $l_N/d = 5$.

Figure 4.- Concluded.

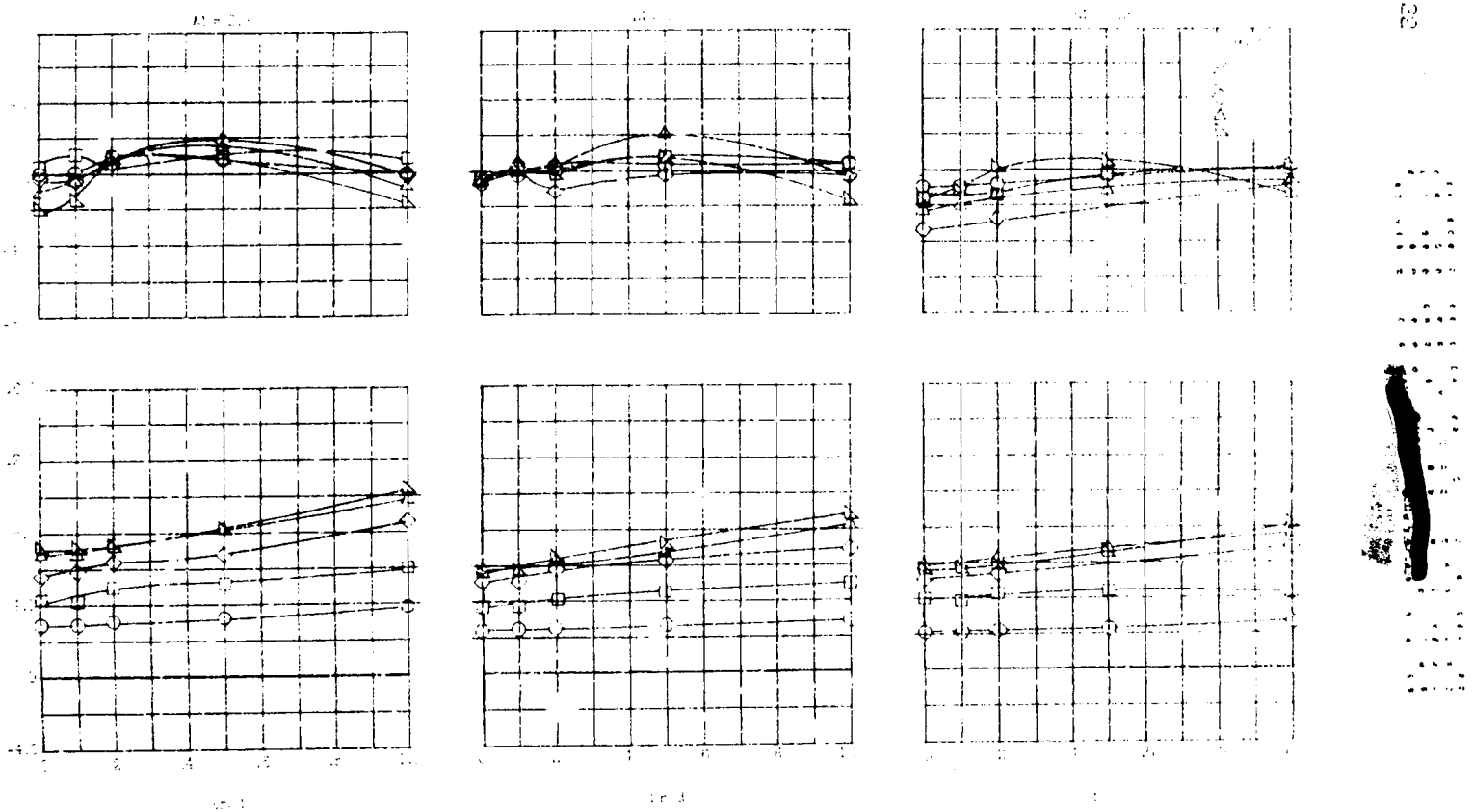

(a) Ogival noses alone. $l/d = l_N/d = 5$.

Figure 5.- Effects of angle of attack on C_m and C_N for fineness-ratio-5 ogival noses with varying nose bluntness with and without a fineness-ratio-2 cylinder afterbody.

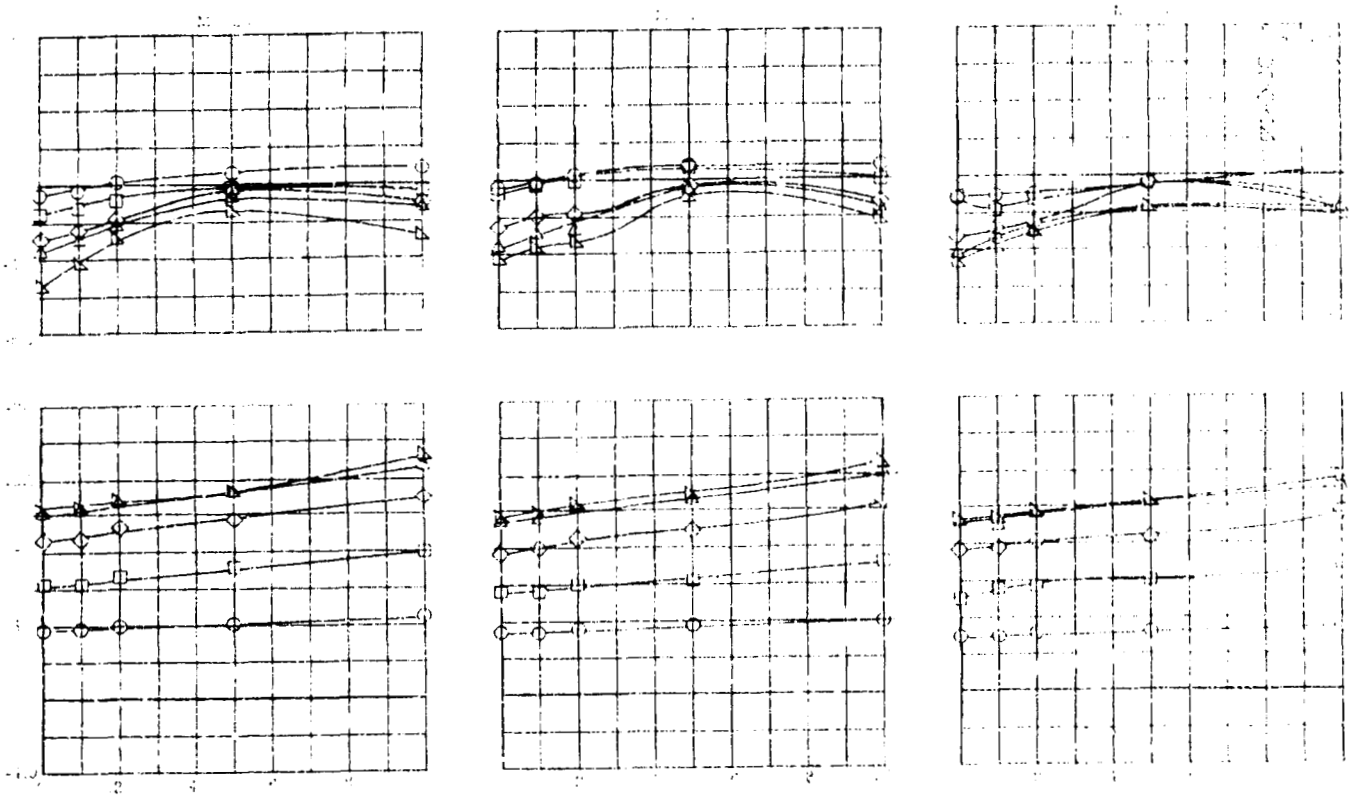

(b) Ogival noses combined with a fineness-ratio-2 cylindrical afterbody. $l/d = 7$; $l_N/d = 5$.

Figure 5.- Concluded.

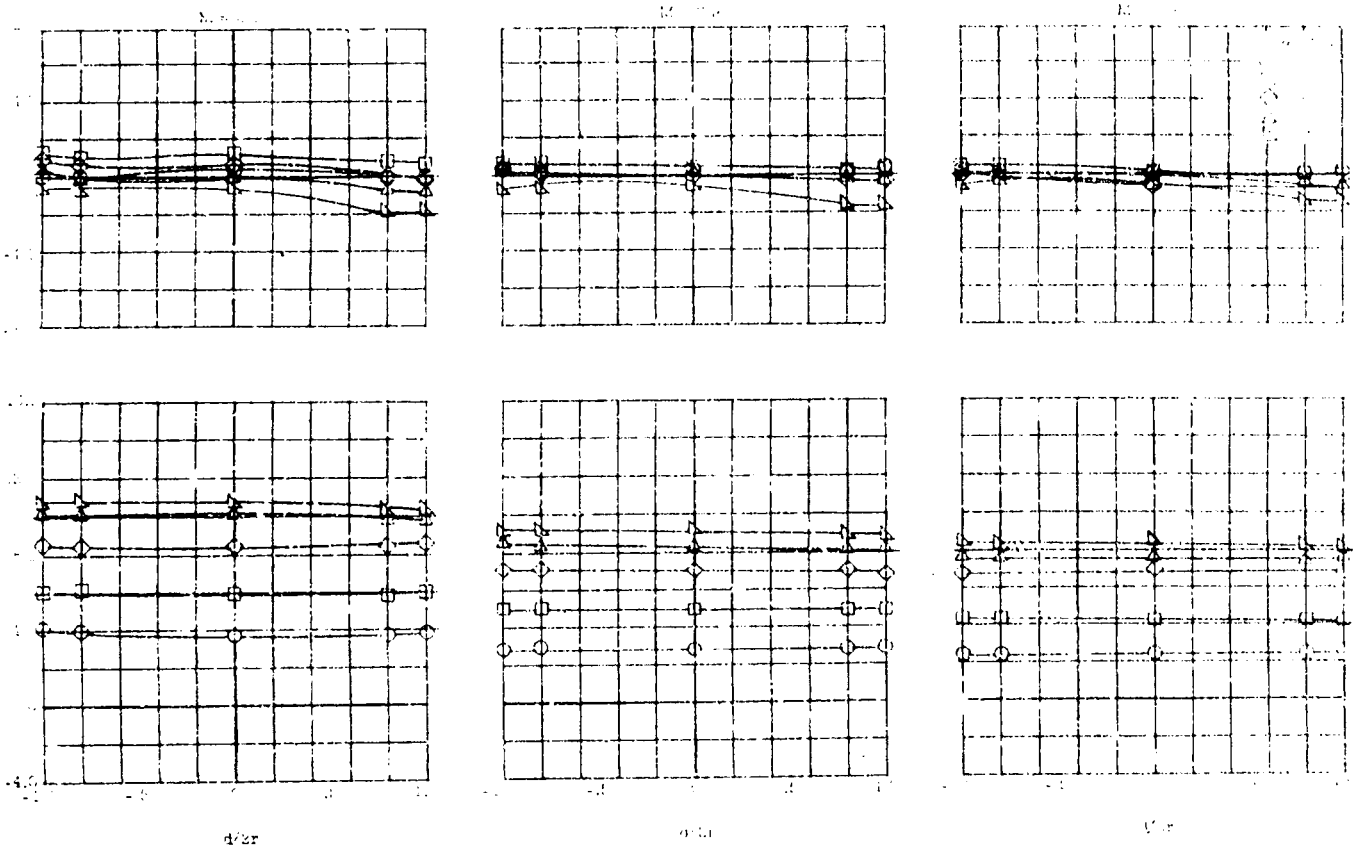

(a) Cylindrical noses alone. $l/d = l_N/d = 5$.

Figure 6.- Effects of angle of attack on C_m and C_N for fineness-ratio-5 cylindrical noses with varying face shape with and without a fineness-ratio-2 cylindrical afterbody.

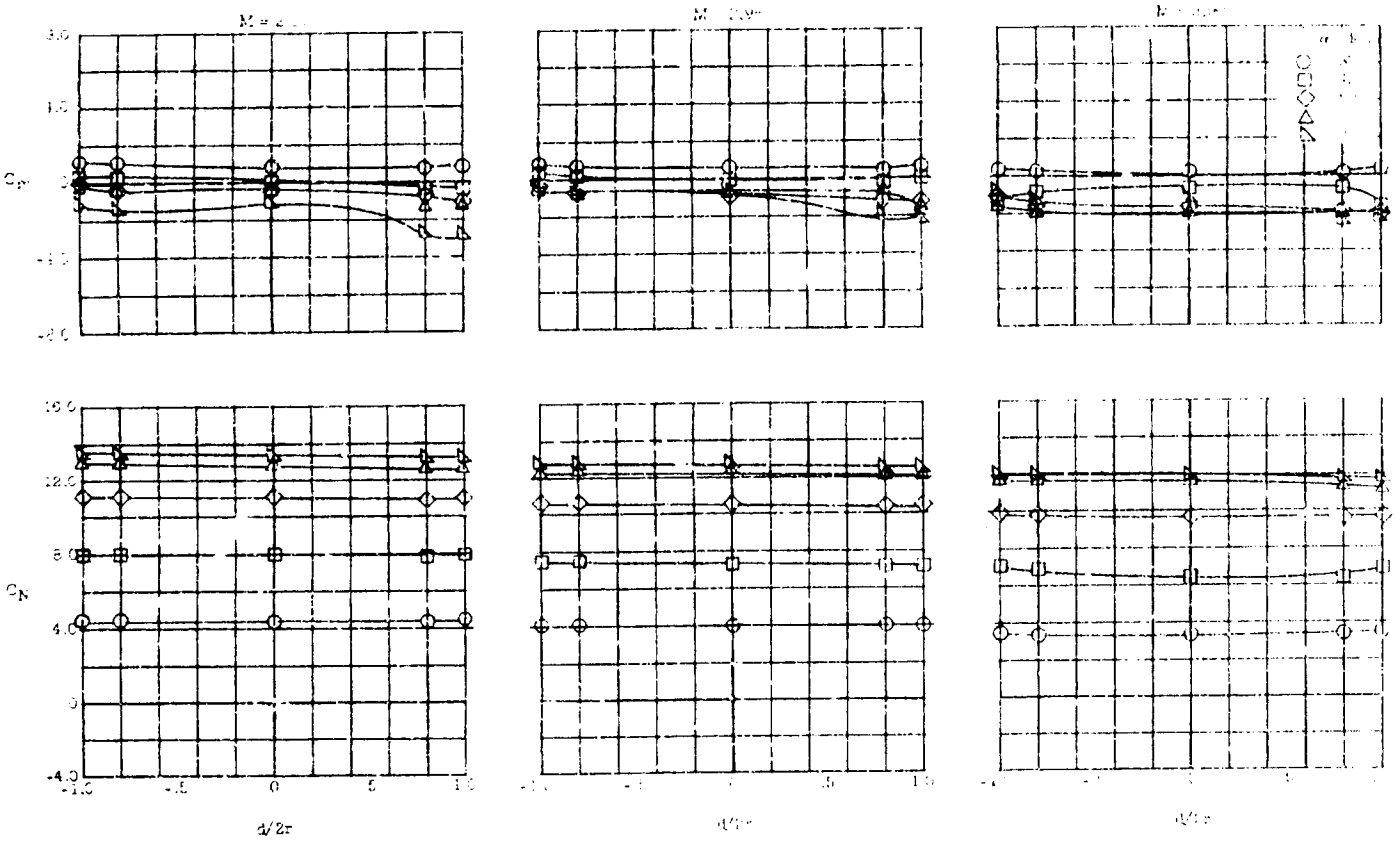

(b) Cylindrical noses combined with a fineness-ratio-2 cylindrical afterbody. $l/d = 7$; $l_N/d = 5$.

Figure 6.- Concluded.

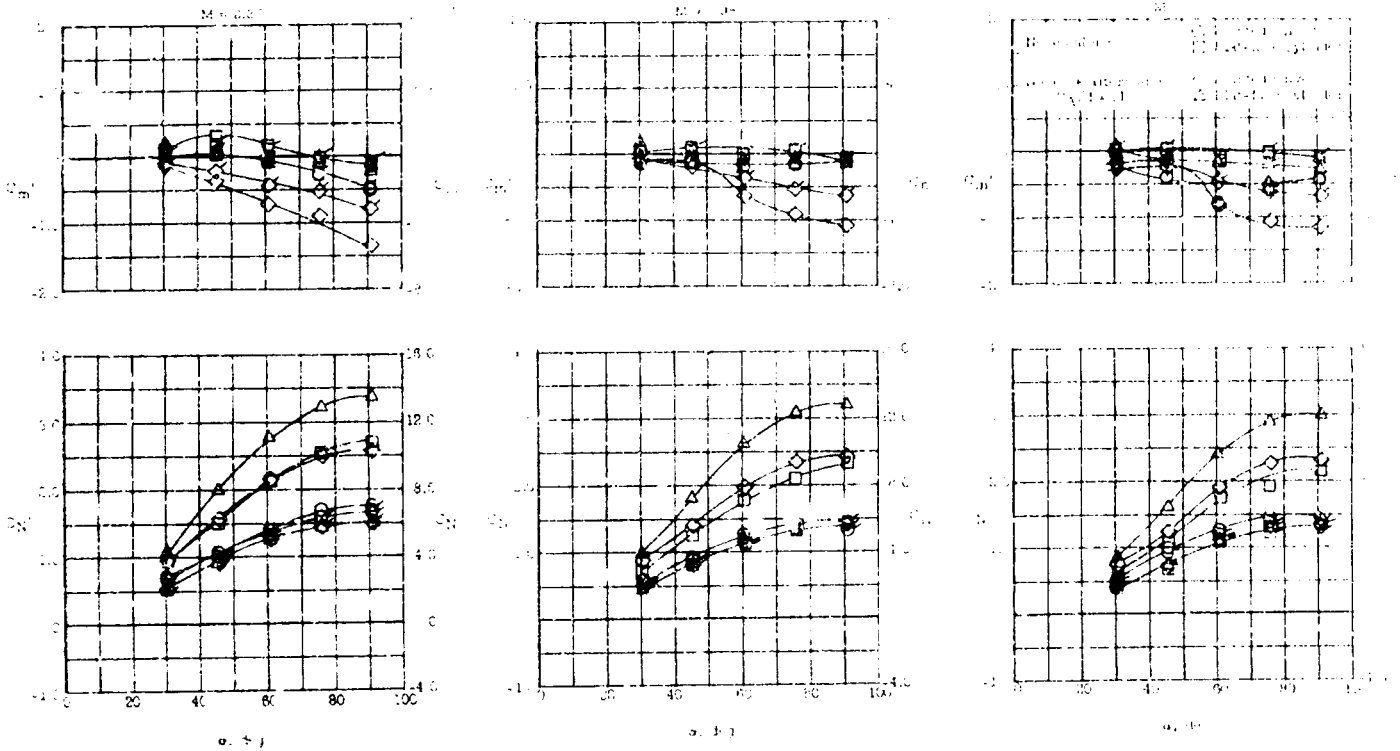

Figure 7.- An example of the use of planform area to correlate experimental C_m and C_N for bodies of revolution, here represented by pointed ogival and flat-face cylindrical noses alone ($l_N/d = 5$) and combined with a fineness-ratio-2 cylindrical afterbody. Flagged symbols represent data referred to body planform area ($C_{m'}$ and $C_{N'}$).

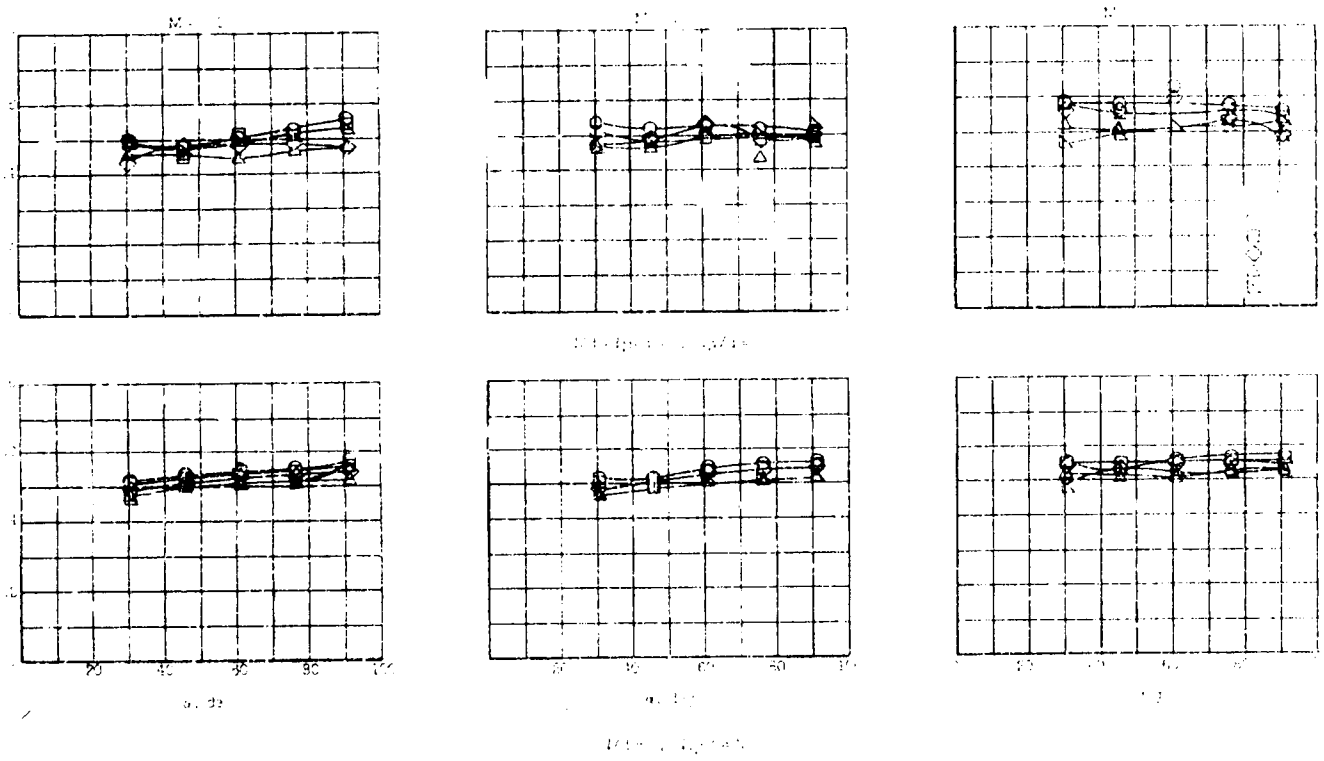

(a) Ogival-nose configurations.

Figure 8.- Effects of ogival-nose bluntness and cylindrical-nose face shape on the centers of pressure of fineness-ratio-5 ogival and cylindrical noses with and without a fineness-ratio-2 cylindrical afterbody.

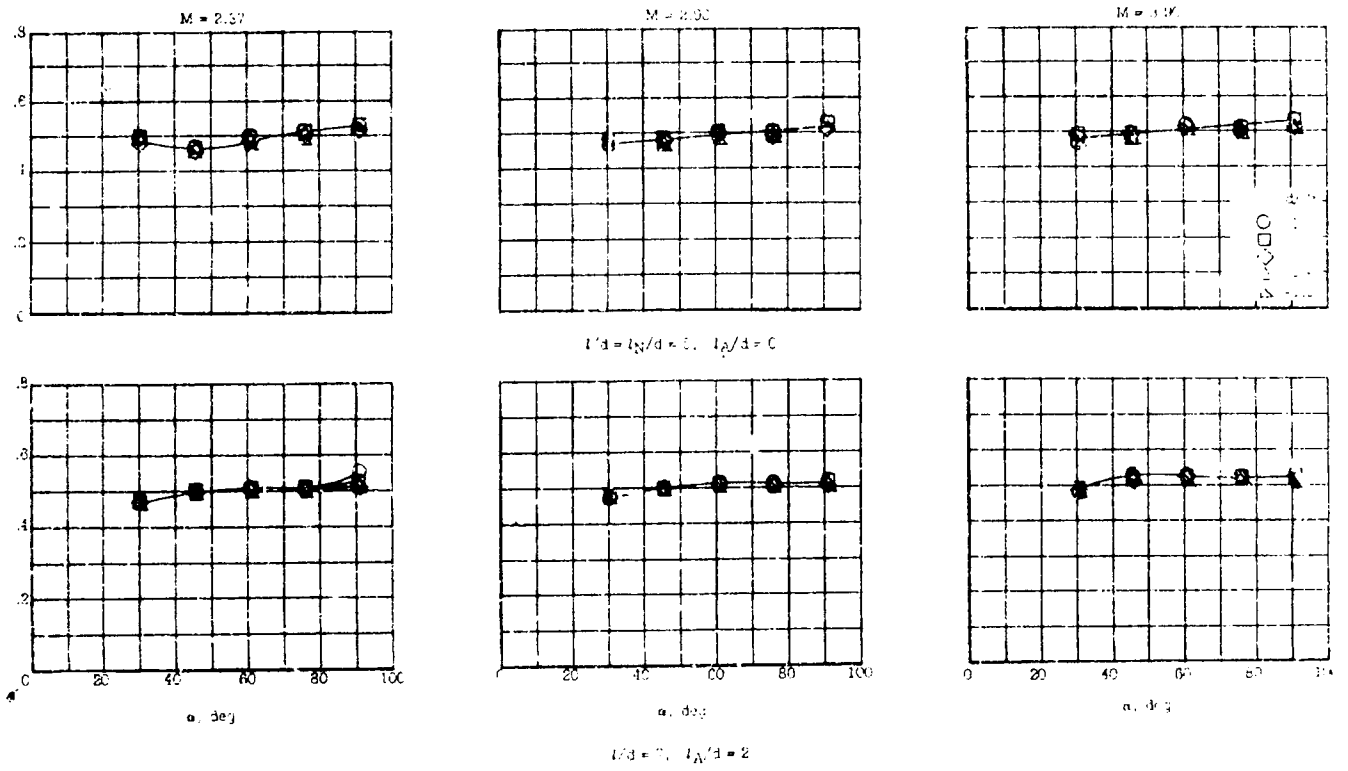

(b) Cylindrical-nose configurations.

Figure 8.- Concluded.

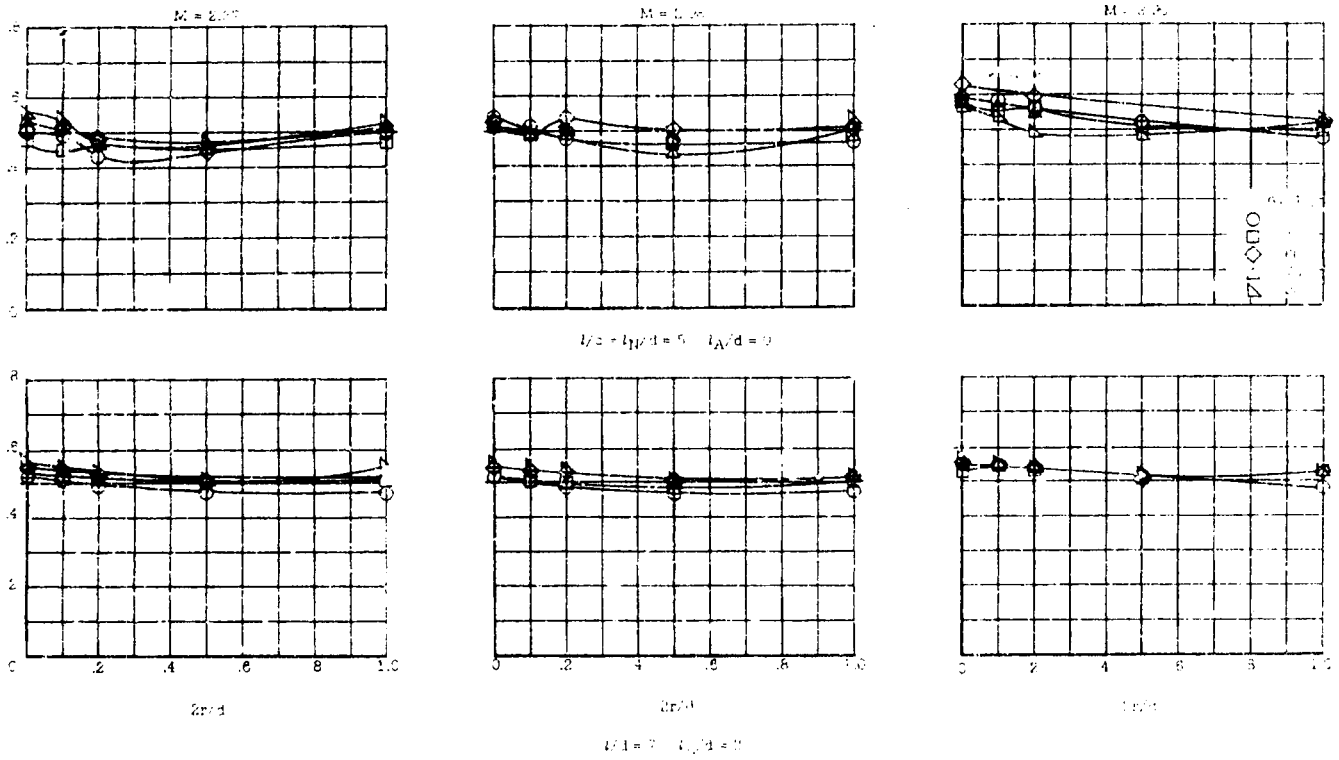

(a) Ogival-nose configurations.

Figure 9.- Effects of angle of attack on the centers of pressure of fineness-ratio-5 ogival and cylindrical noses with and without a fineness-ratio-2 cylindrical afterbody with varying ogival-nose bluntness and varying cylindrical-nose face shape.

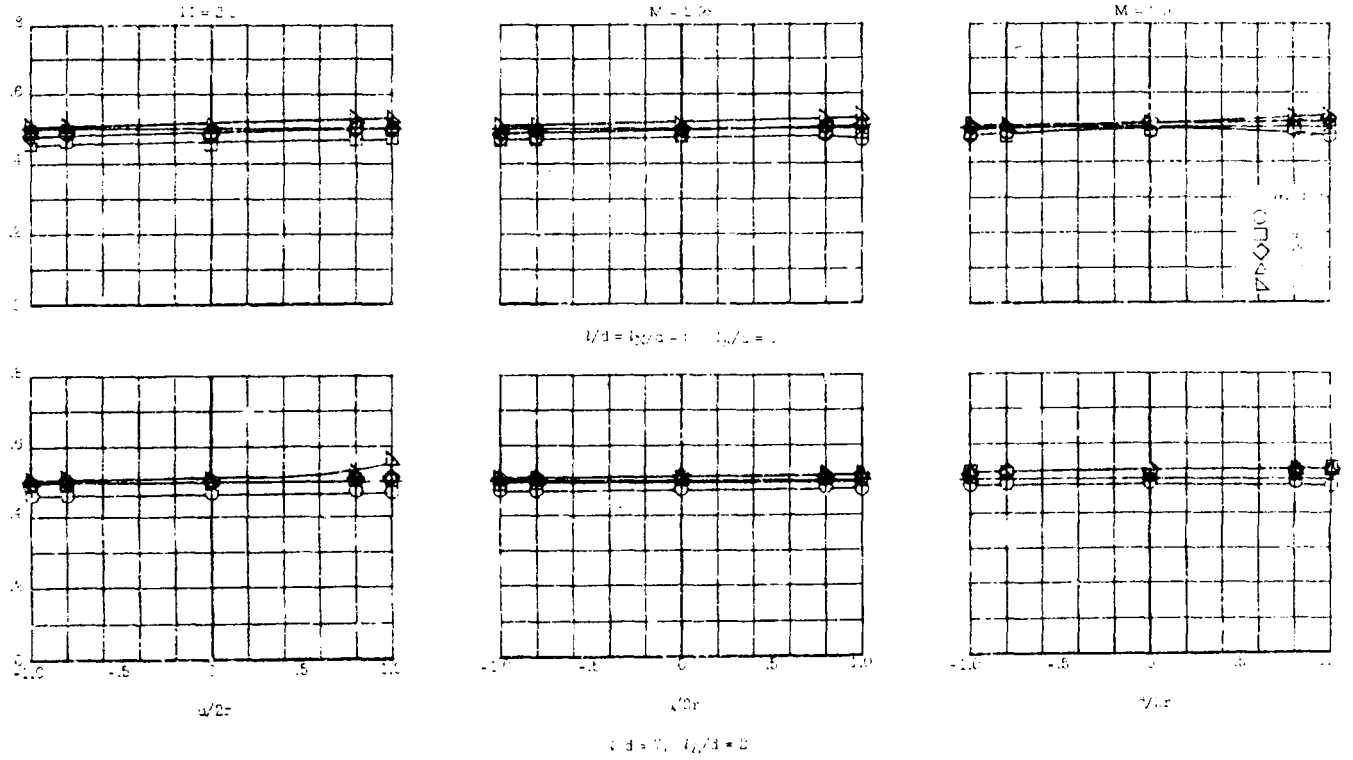

(b) Cylindrical-nose configurations.

Figure 9.- Concluded.

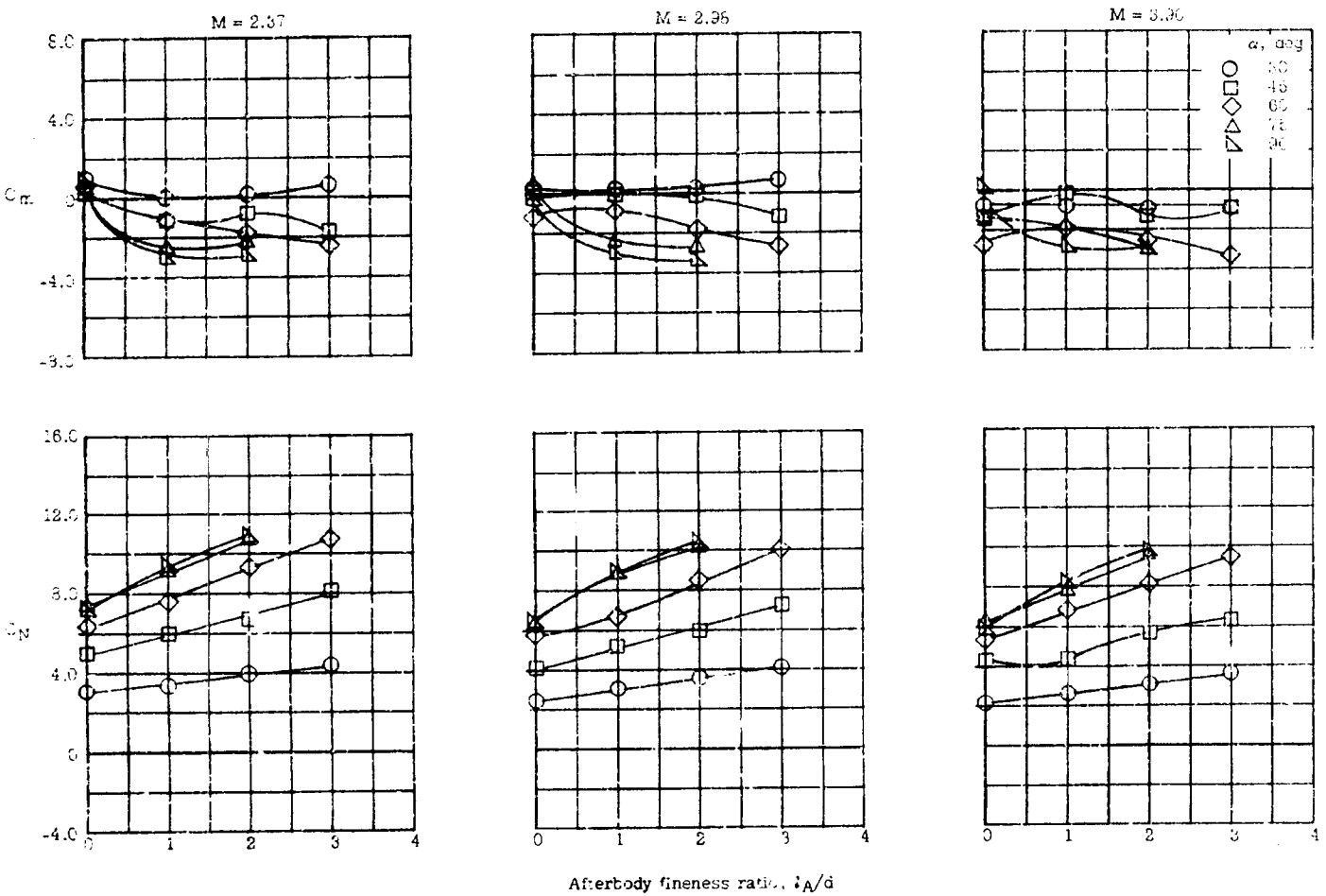

Figure 10.- Effects of angle of attack on C_m and C_N for a fineness-ratio-5 ogival nose with varying afterbody fineness ratio. $2r/d = 0.20$.

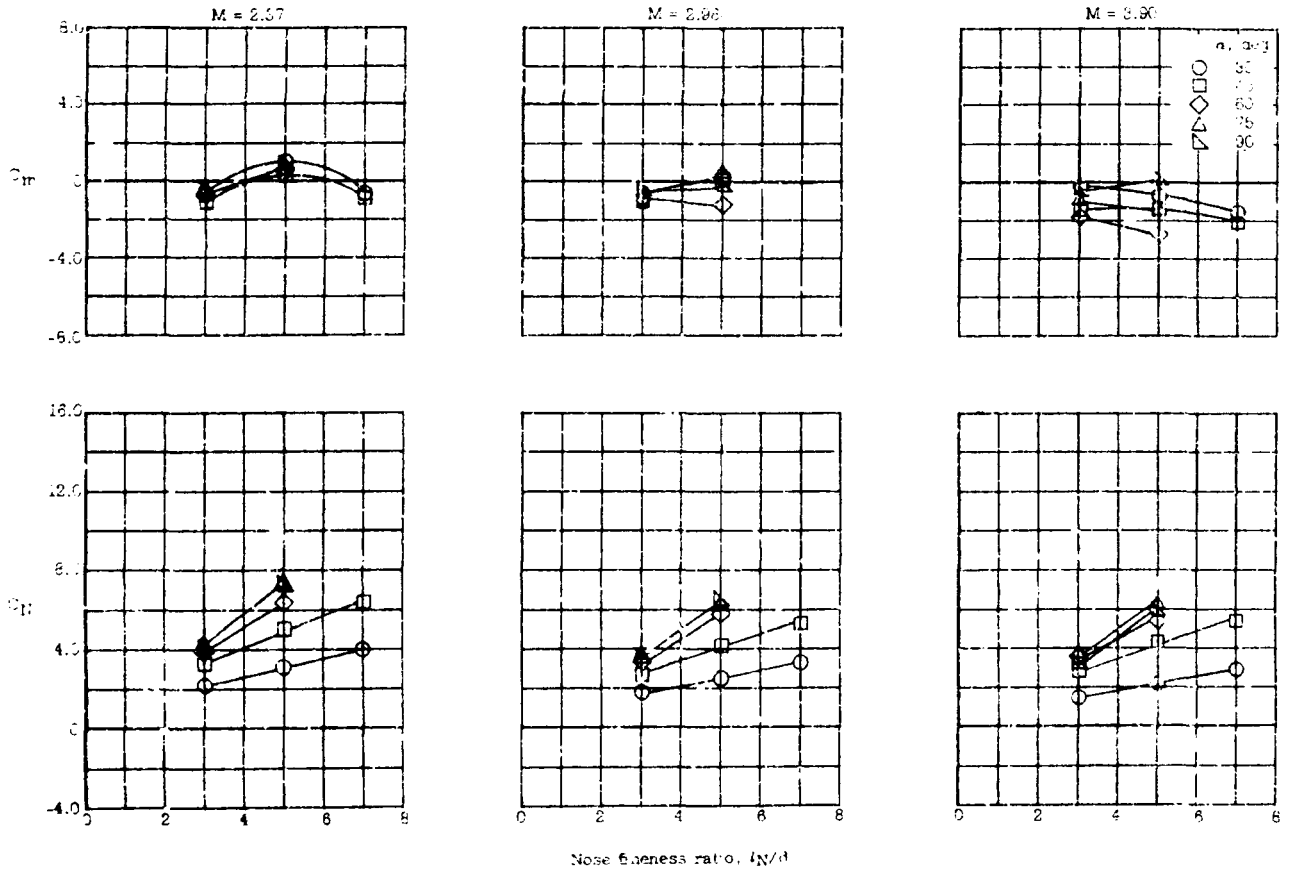

(a) Noses alone; $l_A/d = 0$.

Figure 11.- Effects of angle of attack on C_m and C_N for ogival noses ($2r/d = 0.20$) of varying fineness ratio with and without a fineness-ratio-2 cylindrical afterbody.

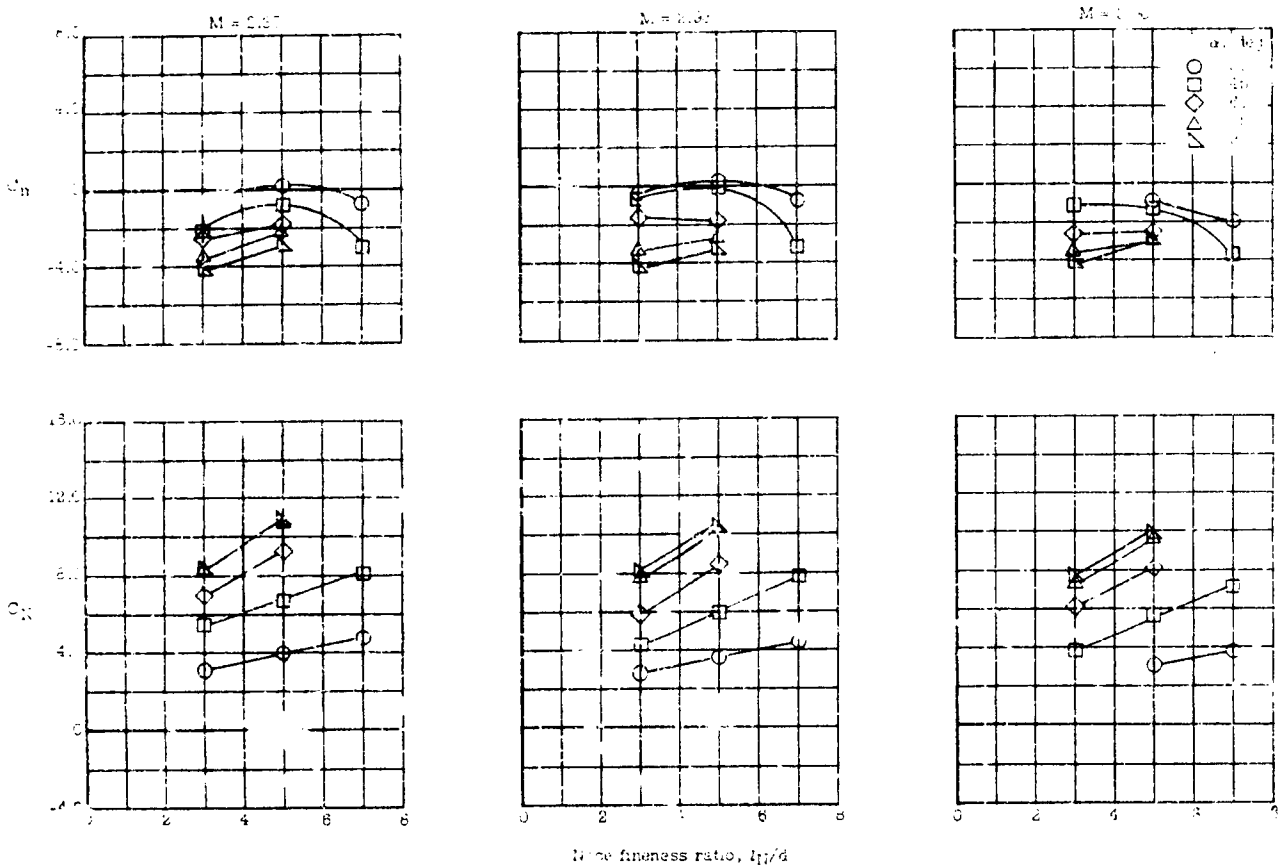

(b) Noses in combination with a fineness-ratio-2 cylindrical afterbody.

Figure 11.- Concluded.

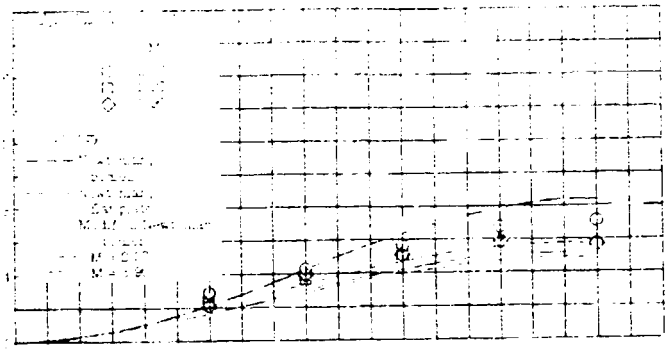

(a) Pointed ogive. $2r/d = 0$; $l/d = l_N/d = 5$.

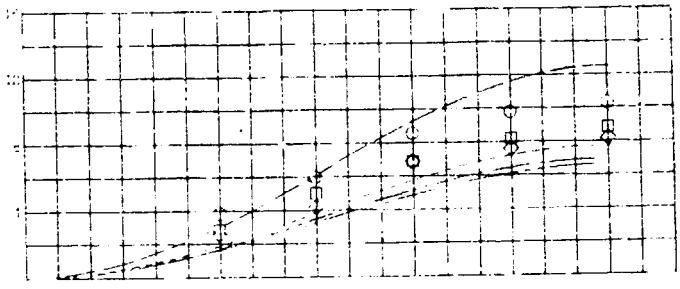

(b) Hemispherical-face cylinder. $d/2r = 1$; $l/d = l_N/d = 5$.

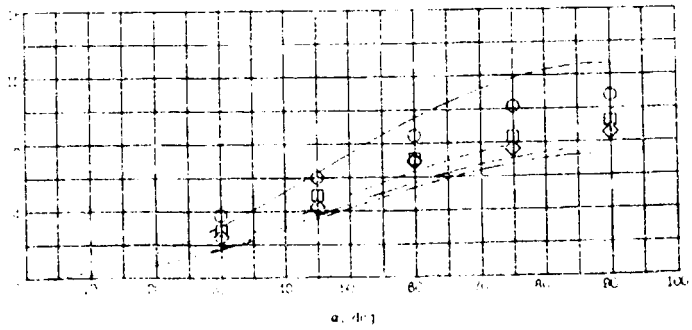

(c) Flat-face cylinder. $d/2r = 0$; $l/d = l_N/d = 5$.

Figure 12.- Experimental and theoretical normal-force coefficients for three fineness-ratio-5 noses representative of the present investigation.

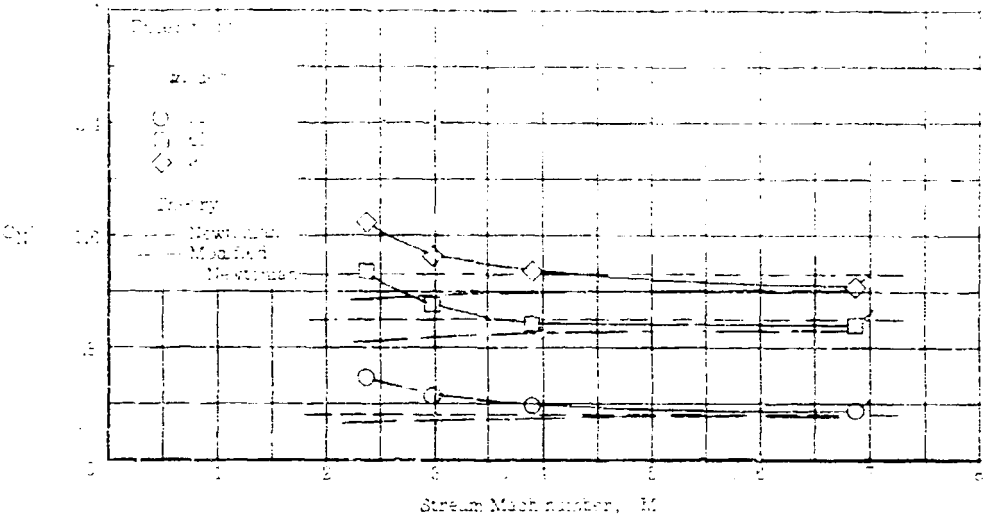

(a) Normal force for a flat-face circular cylinder.

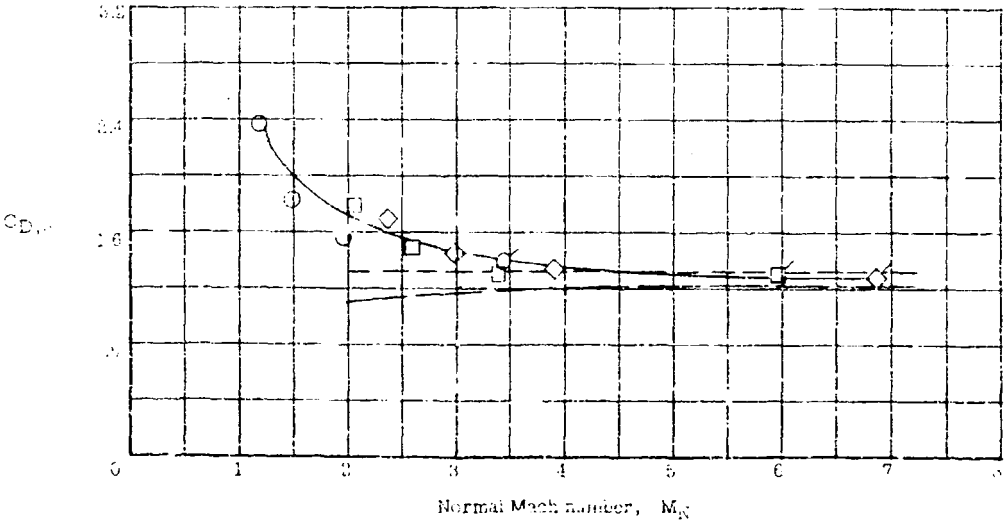

(b) Cross-flow drag for a flat-face circular cylinder.

Figure 13.- Correlation of experimental normal-force data for a flat-face circular cylinder using the cross-flow drag coefficients and the normal Mach number. Flagged symbols represent data from reference 10.